Revised mineral dust emissions in the atmospheric chemistry-climate model EMAC (based on MESSy 2.52)

Klaus Klingmüller[1], Swen Metzger[2], Mohamed Abdelkader[1,3], Vlassis A. Karydis[1], Georgiy L. Stenchikov[3], Andrea Pozzer[1], and Jos Lelieveld[1,2]

[1]Max Planck Institute for Chemistry, P.O. Box 3060, 55020 Mainz, Germany

[2]The Cyprus Institute, P.O. Box 27456, 1645 Nicosia, Cyprus

[3]King Abdullah University of Science and Technology, Thuwal 23955-6900, Saudi Arabia

Correspondence to: Klaus Klingmüller (k.klingmueller@mpic.de)

Abstract. To improve the aeolian dust budget calculations with the global ECHAM/MESSy atmospheric chemistry-climate model (EMAC) we have implemented new input data and updates of the emission scheme.

The data set comprises landcover classification, vegetation, clay fraction and topography. It is based on up-to-date observations, which is crucial to account for the rapid changes of deserts and semi-arid regions in recent decades. The new Moderate-resolution Imaging Spectroradiometer (MODIS) based landcover and vegetation data is time dependent, and the effect of long-term trends and variability of the relevant parameters is therefore considered by the emission scheme. All input data has a spatial resolution of at least $0.1°$ compared to $1°$ in the previous version, equipping the model for high resolution simulations.

We validate the updates by comparing results for the aerosol optical depth (AOD) at 550 nm wavelength from a one year simulation at T106 (about $1.1°$) resolution with Aerosol Robotic Network (AERONET) and MODIS observations, and results for 10 μm dust AOD (DAOD) with Infrared Atmospheric Sounding Interferometer (IASI) retrievals. The update significantly improves agreement with the observations and is therefore recommended to be used in future simulations.

1 Introduction

Aeolian dust can impair everyday life and air quality especially in severe dust storms. Due to the worldwide presence of dust sources and through long range transport it has a significant global impact on atmospheric radiation transfer and air quality, affecting climate (IPCC, 2014) and human health (Giannadaki et al., 2014), which requires detailed representation in general circulation models.

The global ECHAM/MESSy atmospheric chemistry-climate model (EMAC) (Jöckel et al., 2005, 2010) provides a choice of dust emission schemes (Tegen, 2002; Balkanski et al., 2004; Astitha et al., 2012) to calculate the emission flux online based on the meteorological conditions.

An advanced scheme producing convincing results when compared to observations has been presented by Astitha et al.
(2012) building on previous studies (Pérez et al., 2006; Spyrou et al., 2010; Laurent et al., 2008, 2010; Marticorena et al., 1997; Zender et al., 2003; Tegen, 2002), and is the basis of the work presented here. This emission scheme combines meteorological parameters with descriptions of landcover type, clay fraction of the soil and vegetation cover. One variant of the scheme (DU_Astitha2) additionally accounts for regional differences of the particle size distribution, while in the present study we focus on the simpler variant DU_Astitha1, which achieves competitive results with reduced complexity (Astitha et al., 2012) and has proven to perform well in previous studies (Abdelkader et al., 2015, 2016). The emission scheme is summarised in appendix A.

The emission scheme applies physical principles in the sense that the governing equations are derived for microphysical processes that are consistently applied globally without the option to adjust the resulting emissions regionally. In this study we extend the emission scheme by including a topography factor while we strictly adhere to the global consistency concept and refrain from using regional tuning factors.

Though generally the emission scheme produces convincing results, some shortcomings, predominantly related to the input data, have become apparent recently and are the motivation for the revision presented in this study. The original input data for land cover and vegetation is based on observations from the early 1990s and is thus dated in view of the rapid changes of deserts and semi-arid regions in recent decades. For instance, the emission mask resulting from the land cover data considerably limits emissions in the Middle East, essentially not allowing dust emissions in Syria and northern Iraq. This is in conflict with the emergence of severe dust outbreaks from that region (Solomos et al., 2016), and the strong link between the soil conditions in that region and trends of atmospheric dust over the Middle East (Klingmüller et al., 2016). Moreover, only a static land cover map and a single seasonal cycle for the vegetation index was provided.

As a consequence, the effect of variations and trends of these quantities on the modelled dust emissions have been excluded. Further, the resolution of the original input data is limited to $1°$. Particularly for EMAC simulations focusing on dust modelling, high model resolutions are desirable, considering how localised dust outbreaks can occur. In the long term, the resolution of global models will approach the resolution of today's regional models where high resolution input data are essential to include details of dust generation patterns (Shi et al., 2016; Anisimov et al., 2017). For model resolutions higher than T106 ($\approx 1.1°$) as applied in the present study, improved input data is required to justify the numerical effort.

In addition to updated input data addressing these issues, we present adjustments to the emission scheme to assure that the updated input has no undesirable effects such as too strong emissions in mountainous regions and to further improve the performance of the scheme.

To quantify the impact of the updates, we compare a validation simulation with the reference simulation, the latter using the original emission scheme and data. Results and comparisons of other schemes in EMAC are provided elsewhere (Gläser et al., 2012; Astitha et al., 2012). The purpose of the validation is to demonstrate the advantages of the updates and to test the results

so that the modifications can swiftly be adopted by the community; more applications and in depth analysis thereof are beyond the scope of this mostly technical study.

The article is structured as follows: in Sect. 2 we introduce and discuss the updated input data; the modifications to the EMAC code are presented in Sect. 3. The effect of both is validated in Sect. 4 by comparing with the reference simulation, as well as ground based aerosol optical depth (AOD) observations (Sect. 4.1), and satellite based AOD (Sect. 4.2) and dust AOD (DAOD) (Sect. 4.3) retrievals.

2 Updated input data

2.1 Landcover

To replace the landcover classification map of Olson (1992), we use the MODIS MCD12C1 landcover product (MODIS MCD12C1) at $0.05°$ resolution, allowing for dust emissions from regions classified as *barren or sparsely vegetated*. Not only the resolution is higher than for the Olson data, which in the original emission scheme has been used at $1°$ latitude and longitude (aggregated from $10'$), but also yearly updated data from 2001 to 2012 are provided, also expecting more recent updates to become available. Therefore, changes of the landcover for example due to desertification are taken into account, which have not been considered previously. To assess these changes, we compute for each pixel the Kendall rank correlation coefficient τ of annual mask value, which can be either 0 (non-emitting) or 1 (emitting), and time; the result is shown in Fig. 1. Positive values of τ indicate an expansion of source regions to the respective pixel, negative values a disappearance of sources. In some regions the deserts are shrinking, e.g. in the Sahel, Central Asia and Australia. Expanding source areas are found rather centrally in the dust belt, e.g. in the Sahara, on both sides of the Red Sea and north of the Arabian Peninsula in Syria and Iraq.

2.2 Vegetation

Yuan et al. (2011) have reprocessed the MODIS leaf area index (LAI) products to provide a temporally continuous and spatially consistent LAI data set for climate modelling that encompasses the time period since 2000. We have aggregated this data from 30" to $0.1°$ spatial resolution and from eight-day to one month temporal resolution. The data replaces the twelve month seasonal cycle of the vegetation area index with $1°$ resolution based on the work of Kergoat et al. (1999) and Bonan et al. (2002). Using continually updated monthly values instead of a repeating seasonal cycle implies that multi-annual vegetation trends are taken into account.

The LAI data is used to compute the vegetation factor,

$$f_{\text{veg}} = 1 - \frac{\min(\text{LAI}, 0.35)}{0.35}. \tag{1}$$

The 16 year average, standard deviation of the yearly averages and the trend of the vegetation factor are shown in Fig. 2. The trend has been calulated based on the annual averages using linear regression; only pixels with p values below the significance level of 0.05 are plotted. As demonstrated by the standard deviation plot, large variability and trends, e.g. related to changing

desert boundaries, coincident with the regions of landcover changes, as shown in Fig. 1 can strongly influence the results. The strongest variability is observed in the interior lowlands of Australia (Simpson, Strzelecki and Tirari Deserts), the Thar Desert (India/Pakistan) and Mesopotamia. While in Australia the variability does not yield a significant trend over the 16 year period, in and around the Thar desert a strong decrease of the vegetation factor, indicating vegetation growth, is observed. This inhibits

5   dust emissions and could result in the significant negative AOD trend in that region reported by Klingmüller et al. (2016). In contrast, vegetation decreases in Syria and Iraq, resulting in a larger vegetation factor and more dust emissions. However, similar to Australia, considering the strong variability, the trend is not very distinct because the highest vegetation factor in Iraq and Syria occurred in 2008 in the middle of the period of available data, whereas it decreased again in recent years.

2.3   Clay fraction

10   The efficiency of the sandblasting process is very sensitive to the clay fraction of the surface soil. Both very small and very large clay fractions are assumed to suppress the sandblasting efficiency. Our parametrisation of this dependency is discussed in section 3. Replacing the $1°$ clay fraction map of Scholes and Brown de Colstoun (2011), here we employ higher resolved clay fraction data from the *Global Soil Dataset for use in Earth System Models* (GSDE) (Shangguan et al., 2014), aggregated from 30" to $0.1°$. The GSDE provides the clay fraction of the topmost 4.5 cm soil layer, which is most relevant for sandblasting

15   rather than the clay fraction of the topmost 30 cm in the data of Scholes and Brown de Colstoun (2011).

3   Modifications to the emission scheme

Sandblasting efficiency: The sandblasting efficiency used by Astitha et al. (2012), based on the studies of Marticorena and Bergametti (1995) and Tegen (2002), increases exponentially with a clay fraction up to 20 %, beyond which the sandblasting is negligible, see Fig. 3. The resulting threshold is problematic in regions where the clay fraction is in the range of this discontinu-

20   ity, for example in Iraq and Syria: small variations in the clay fraction can drastically alter the sandblasting efficiency between its maximum and essentially zero. Considering that both the clay fraction data and the sandblasting efficiency measurements are associated with uncertainty, we propose to apply a Gaussian filter. Figure 3 shows the efficiency after applying a filter with an interquartile range of 5 %, which is used in the validation simulation discussed below. The filter width could be optimised systematically, but in our experience results are robust by smoothing the distinct peak at 20 % clay fraction. Combining the

25   filtered sandblasting efficiency with the updated clay fraction data (section 2.3) yields the global map presented in Fig. 4.

    Soil moisture term: The original emission scheme of Astitha et al. (2012) applies a soil moisture dependent correction factor to the threshold friction velocity which increases the threshold and thus reduces dust emissions from wet soils. This correction factor has not been active in MESSy versions up to 2.52 and since the higher AOD over the Middle East obtained without the factor generally more closely resembles the satellite observations, it is not used in the present study. Nevertheless, the monthly

30   vegetation data described above accounts for secondary effects of soil moisture variations via the vegetation factor. However, since the soil moisture strongly correlates with the AOD over the Middle East (Klingmüller et al., 2016), suggesting a direct link between surface drying and increasing dust emissions, we consider a detailed parametrisation of the soil moisture effect

to be essential to capture the observed trends in future simulations. This will require a comprehensive soil model providing accurate moisture values for the topmost surface layer.

Surface friction velocity limit: The relation of the horizontal dust particle flux H and the surface friction velocity u_* is parametrised as a polynomial of degree 3,

$$H \propto (u_* + u_{*t})^2 (u_* - u_{*t}), \tag{2}$$

where u_{*t} is the threshold friction-velocity. Therefore, high surface friction velocities occurring in mountainous regions can produce spuriously strong dust outbreaks where emissions are not limited by the updated landcover mask, vegetation factor or sandblasting efficiency, e.g. in Iran. To avoid this, we limit the threshold friction velocity in the above equation to a maximum value of 0.4 m / s. The limit might be further adjusted but the given value yields good results as shown in Sect. 4.

Topography factor: In the original scheme, the accumulation of sediments in valleys and depressions is not considered explicitly and is only to some extent reflected implicitly by other input data such as the clay fraction. As shown by the reference simulation presented in Sect. 4, this can result in an underestimation of dust emissions from areas like the Tigris-Euphrates Basin. We therefore include a topography factor using the topographic source function proposed by Ginoux et al. (2001),

$$S_{\mathrm{topo}} = \left(\frac{z_{\max} - z}{z_{\max} - z_{\min}} \right)^5, \tag{3}$$

where z is the median elevation in a circle with $1°$ diameter and $z_{\min}$ ($z_{\max}$) the minimum (maximum) elevation in the surrounding circle with $10°$ diameter. (Ginoux et al. (2001) use $1°$ pixels and the extreme values in the surrounding $10° \times 10°$ square). The Global Multi-resolution Terrain Elevation Data 2010 (GMTED2010) (Danielson and Gesch, 2011; GMTED2010, 2010) is used as topography data base. Figure 5 depicts a global map of the resulting topography factor. As the topography factor takes values between 0 and 1, a normalisation factor $N \geq 1$ has to be multiplied to conserve the global emissions. Based on a one-month test simulation we use $N = 5.3$.

Mode mapping: The emission scheme considers emissions into three log-normal modes, adapting the parameters of the "background" modes of d'Almeida (1987) listed in table 2. Originally, these log-normal modes have been mapped to eight transport bins as used by Pérez et al. (2006), before being distributed to the accumulation and coarse mode of the EMAC aerosol submodel GMXE. We simplify this procedure by directly mapping the three emission modes to the two relevant GMXE modes. The mass fraction M assigned to each GMXE mode is

$$M = \sum_{i=1}^{3} \frac{1}{2} \left(\mathrm{erf}(\frac{\ln(d_{\max}/\tilde{d}_i)}{\sqrt{2}\ln\sigma_{g,i}}) - \mathrm{erf}(\frac{\ln(d_{\min}/\tilde{d}_i)}{\sqrt{2}\ln\sigma_{g,i}}) \right), \tag{4}$$

where the sum encompasses over the three emission modes, $\tilde{d}_i$ and $\sigma_{g,i}$ are the mass median diameter and geometric standard deviation of each emission mode, and $d_{\min}$ and $d_{\max}$ are the threshold diameters of the GMXE mode. In practice, the modification is equivalent to a change of the threshold diameter between accumulation and coarse mode, which is now consistent

with the GMXE parameters. Moreover, the algorithm generalises seamlessly when including additional GMXE modes such as a giant aerosol mode ($> 10 \mu$m).

Scaling factor: For the dimensionless empirical constant c by which the horizontal particle flux is scaled, Astitha et al. (2012) use the value $c = 1$, consistent with Darmenova et al. (2009). Since the dust emissions, especially in the Middled East,

5   tend to underestimate the observations, we increase the value to $c = 1.5$, which is bounded by the original value and $c = 2.61$ used by White (1979) and Marticorena and Bergametti (1995). As will be discussed in section 4, with this value we obtain the same total amount of globally emitted dust as with the original emission scheme by Astitha et al. (2012). It should be stressed that the scaling factor is the central empirical tuning parameter of the emission scheme and might be improved by systematic optimisation, but our focus is on the spatiotemporal emission pattern which is largely unaffected by the overall scaling.

10   *Chemical composition:* In addition to the bulk dust flux output, we compute the Na^+, K^+, Ca^{++} and Mg^{++} fractions of the emitted dust, since mineral cations are important for the gas-aerosol partitioning (Metzger et al., 2006). For this purpose we have generated maps of the desert soil composition (Fig. 6) based on the fractions reported by Karydis et al. (2016) and geographical data from the Natural Earth dataset (Natural Earth, 2016). The chemical composition does not affect the amount of dust emitted, but the chemical ageing of airborne dust particles simulated by the GMXE submodel can affect the atmospheric

15   residence time (Abdelkader et al., 2015) and the optical properties (Klingmüller et al., 2014).

4 Validation

We use EMAC in the combination ECHAM 5.3.02 and MESSy 2.52 at horizontal resolution T106 with 31 vertical levels. The Gaussian T106 grid has a grid spacing of $1.125°$ along the latitudes and about $1.121°$ along the longitudes. At the equator, this corresponds to virtually quadratical cells with around 125 km edge length. The following MESSy submodels have

20   been enabled: AEROPT, AIRSEA, CLOUD, CLOUDOPT, CONVECT, CVTRANS, DDEP, GMXE, JVAL, LNOX, MECCA, OFFEMIS, ONEMIS, ORBIT, ORACLE, PTRAC, RAD, SCAV, SEDI, SURFACE, TNUDGE, TROPOP. The dust emission scheme is evaluated by the online emission submodel ONEMIS, the aerosol microphysical processes are simulated by the Global Model aerosol eXtEnsion (GMXE) submodel (Pringle et al., 2010a, b). Within GMXE two gas-aerosol partitioning schemes are available, ISOROPIA II (Fountoukis and Nenes, 2007) and EQSAM4clim (Metzger et al., 2016), here we employ

25   the former. The prognostic radiative-transfer calculation uses the Tanre aerosol climatology (Tanre et al., 1984), and the model dynamics above the boundary layer are nudged to meteorological analyses of the European Centre for Medium-Range Weather Forecasts (ECMWF). The CMIP5 (Coupled Model Intercomparison Project), GFEDv3.1 (Global Fire Emissions Database) and AeroCom (Aerosol Comparisons between Observations and Models) databases provide anthropogenic, biomass burning and sea salt emissions, respectively.

30   Two simulations are considered: a reference simulation using the original emission scheme and a validation simulation using the updated input data presented in Sect. 2 and the modifications presented in Sect. 3. The chemical composition of the emitted particles is considered in both simulations. As validation time period we selected the year 2011. The simulations are

initialised at 1 July 2010 from the output of a lower resolving T42 simulation starting in 1998. After this initialisation, six months simulated with the final T106 resolution serve as additional spin-up period.

To quantify the (dis)agreement of model results and observations we use the skill score S defined by Taylor (2001),

$$S = \frac{4(1+r)^4}{(\sigma_1/\sigma_2 + \sigma_2/\sigma_1)^2(1+r_0)^4}, \tag{5}$$

5 where r is the correlation coefficient and σ_1 and σ_2 are the standard deviations of modelled and observed values. As maximum attainable correlation coefficient we simply use $r_0 = 1$ since we are predominantly interested in the relative changes of the skill score resulting from our modifications to the dust emission scheme. A more accurate estimate $r_0 < 1$ would result in higher skill scores.

Both simulations obtain the same global mineral dust emission of 1.3 Gt in 2011 (Table 3), which is well in the range

10 of values reported by Huneeus et al. (2011) and close to their median of 1.1 Gt per year. Aligning the threshold between accumulation and coarse mode with GMXE as described in section 3 for the parameters shown in Table 2 results in more accumulation mode emissions in the validation simulation (0.15 Gt / year) than in the reference simulation (0.052 Gt / year), thus higher 550 nm AOD values are expected in the former.

4.1 AERONET

15 For the comparison with Aerosol Robotic Network (AERONET) (Holben et al., 1998; AERONET) AOD observations, we select regions based on the relevance of the regional dust emissions and the abundance of AERONET stations. We focus on the six regions of interest depicted in Fig. 7 encompassing the Middle East (region A), Africa (B), Central and East Asia (C), the south-west of the United States of America (D), the Southern Cone (E) and Australia (F). All stations with observations during at least 120 days distributed over at least 9 months of 2011 are considered.

20 We compare daily averages of modelled and observed aerosol optical depth (AOD) at 550 nm, where the AERONET AOD at this wavelength is obtained by interpolation using the Ångström exponent. For each station we use the model values from the grid cell covering the station coordinates. The skill score S is shown in Fig. 8. For most stations, the validation simulation achieves higher skill scores than the reference simulation, similar skill scores are obtained for the Australian stations. Only over four stations in north-west Africa the validation simulations produces noticeably lower skill scores than the reference run.

25 However, the skill scores for these stations remain among the highest globally. Moreover, the two stations with the strongest skill score degradation are located very close to each other on the island Tenerife, in Santa Cruz de Tenerife and at the Izana Atmospheric Observatory on Mount Teide. In contrast, the validation skill score for a third station on Tenerife, in La Laguna, is marginally larger than the corresponding reference skill score.

Studying the AOD time series for these three stations (Fig. 9 top), reveals that over Santa Cruz de Tenerife the model slightly

30 overestimates the observations and the even higher AOD levels in the validation simulation result in the lower skill score. On the other hand, dust events observed by AERONET in January and December are reproduced by the validation simulation, but not by the reference simulation. The Izana station on Mount Teide is special: located at 2391 m altitude, it shares the

same model grid cell with the La Laguna station at 568 m altitude, Fig. 9 (bottom), but naturally the observed AOD is much lower. Obviously, the station site is not well represented by the model grid cell, which predominantly covers open sea. These considerations put the regression of the skill score over the Canaries into perspective and suggest that some overestimation of the AOD over north-west Africa in the validation simulation is an acceptable trade-off in view of the skill score increase

5   elsewhere. This conclusion is further supported by the comparison with MODIS observations in the following section.

4.2   MODIS

To verify the global aerosol distribution, we validate the model AOD against observations from the Terra satellite provided by the Moderate-resolution Imaging Spectroradiometer (MODIS) data collection 6 (Hubanks et al., 2015; Levy et al., 2013; MODIS MOD08 M3). We use the merged 550 nm AOD combining retrievals from the Deep Blue and Dark Target algorithms

10   (Sayer et al., 2014).

Figure 10 compares the 2011 annual mean AOD from the two simulations and MODIS. The AOD levels over the Sahara and the Middle East produced by the validation simulation agree well with the observed levels, whereas they are underestimated by the reference simulation. Features of the MODIS distribution found in the validation but not in the reference result are regionally high AOD values over the Middle East along the Gulf and extending over Iraq and Syria, and the absence of a local

15   maximum over Argentina. The latter is even more evident at higher wavelengths considered in the following section. Over west Africa, the high AOD levels in the validation simulation extend slightly further north than observed by MODIS. This is consistent with the overestimation of AERONET observations in that region discussed above, but does not considerably compromise the globally improved agreement with MODIS.

The improved agreement of the AOD distribution obtained by the validation simulation can be quantified by correlating the

20   pixel values of the equivalent maps shown in Fig. 10. The revised dust emissions enhance the spatial correlation of the AOD pattern from 0.79 to 0.81 and the skill score from 0.58 to 0.67.

Fig. 11 zooms into the Middle East (Region A) to illustrate the annual variability of the 550 nm AOD by showing seasonal means. Especially in Spring and Summer, the enhanced AOD levels along the Tigris-Euphrates Basin and the Gulf are clearly visible in the validation result, consistent with the MODIS observations, while not being represented in the reference results.

25   During summer, the validation simulation produces higher AOD levels also over Arabian and Red Sea, which are closer to the extremely high levels reported by MODIS and Brindley et al. (2015). Surprisingly, the MODIS AOD over Iran is close to zero throughout the year, but substantial levels are obtained during spring and summer by both simulations, with higher levels in the validation simulation than in the reference simulation. The strong seasonal cycle over the Middle East observed by MODIS is reproduced by both simulations, but with its higher spring and summer AOD levels, the validation simulation yields a higher

30   amplitude in better agreement with MODIS.

4.3   IASI

To focus the evaluation more tightly on dust, we utilise data from the *Infrared Atmospheric Sounding Interferometer* (IASI) (Clerbaux et al., 2009; Hilton et al., 2012) provided by the Aerosol-CCI (Climate Change Initiative) project (Popp et al., 2016;

IASI) of the *European Space Agency* (ESA). We use version 7 of the level 3 monthly dust AOD (DAOD) at 10 μm prepared at the Université Libre de Bruxelles (IASI_ULB.v7). The corresponding annual average DAOD map for 2011 is shown in the middle panel of Fig. 12.

To compare with the IASI DAOD, we filter the daily 10 μm EMAC AOD considering only dust dominated values as DAOD, setting the DAOD to zero if sea salt dominates instead. The contribution of both components is quantified by weighting the AOD of each mode with the volume fraction of the component. The diagnostic output of optical properties at wavelengths up to 10 μm has not been utilised previously in EMAC though proves very valuable to compare with remotely sensed optical properties of coarse particles such as aeolian dust. The annual average for 2011 from validation and reference simulation are shown in the top and bottom panel of Fig. 12. In several aspects the DAOD distribution obtained by the validation simulation resembles the IASI observations more closely. In the Middle East, the region of high dust loads distinctly extends north-westwards into the Fertile Crescent, whereas comparably low dust loads are found over the western half of the Arabian Peninsula. The DAOD is more pronounced over Pakistan, and similarly over Djibouti and the adjacent regions south-west of the Red Sea. The regional maximum over Chad is less distinct than in the reference simulation. Over the Southern Andes, the maximum obtained by the reference simulation, though not detected by IASI, is not reproduced by the validation simulation, which is distinctly more realistic.

The correlation coefficient of the validation result and IASI is 0.87 compared to 0.79 for the reference simulation, the corresponding skill score is enhanced by our modifications from 0.62 to 0.76.

The annual variability of the 10 μm DAOD over the Middle East (Region A) is compared in Fig. 13. As for the AOD, in spring and summer, the high DAOD values along the Tigris-Euphrates Basin are clearly visible in the validation result, consistent with the IASI observations, while not being represented in the reference result. During summer, the DAOD pattern obtained by the validation simulation at the southern Red Sea resembles the pattern observed by IASI, even though the observed regional maximum is more pronounced. Also the DAOD at the Iranian and Pakistani Arabian Sea coast produced by the validation simulation agrees more closely with the IASI result. The reference simulation does not produce dust over the Caspian Sea and to its south, whereas IASI obtains significant DAOD values in spring and summer. These are reproduced by the validation simulation but seem to be slightly overestimated during summer. The strong seasonal cycle observed by IASI is realistically reproduced by both simulations.

5 Conclusions

We have prepared new input data for use with the EMAC dust emission scheme developed by Astitha et al. (2012), and proposed changes and extensions. With a geographic representation of at least $0.1°$ for all input parameters, the updated input data has a significantly higher spatial resolution than the data used thus far. Therefore, the new data will be important for use in planned high resolution simulations with truncations of T255 or higher (< 50km). The land cover and vegetation in the updated data is time dependent, so that the effect of long-term trends and variability of these quantities on the dust emissions are taken into account. In addition to the input parameters used by the original implementation by Astitha et al. (2012), we take

the topography into account, which enhances the emissions from basins and valleys such as the Tigris-Euphrates region and the Afar Triangle, in better agreement with observations. Moreover, we have produced soil composition maps to differentiate the chemical composition of dust particles from different deserts that affects the coating of mineral dust by hygroscopic salts during atmospheric ageing.

5   The updated input data in combination with the adjustments to the emission scheme improve the modelled AOD and DAOD, as demonstrated by the comparison with AERONET, MODIS and IASI observations. For this validation, we have evaluated the EMAC DAOD at wavelengths up to $10\ \mu$m for the first time, which allows testing of the model with a focus on dust, i.e. based on IASI DAOD.

    While the updates clearly improve the global distribution of aeolian dust, the total amount of globally emitted dust remains
10 unchanged and consistent with literature values.

Code and data availability

The input data files and all modifications to the EMAC source code presented in this article are available on request.

Acknowledgements. The research reported in this publication has received funding from the King Abdullah University of Science and Technology (KAUST) CRG3 grant URF/1/2180-01 *Combined Radiative and Air Quality Effects of Anthropogenic Air Pollution and Dust over*
15 *the Arabian Peninsula*. S. Metzger receives funding from the European Commission through the H2020-EINFRA-2015-1 project "Energy oriented Centre of Excellence for computer applications (EoCoE)", Proposal number: 676629.

Appendix A: Emission equation

In the DU_Astitha1 emission scheme (Astitha et al., 2012), the threshold surface friction velocity u_{*t} is obtained by the equation

$$
u_{*t} = 0.129 \sqrt{\frac{D_{\mathrm{p}}}{\rho_{\mathrm{air}}} \left(\rho_{\mathrm{p}} g + \frac{0.006\mathrm{g}\sqrt{\mathrm{cm}}/\mathrm{s}^2}{D_{\mathrm{p}}^{5/2}} \right)}
$$

$$
\times \begin{cases} \frac{1}{\sqrt{1.928 B^{0.092} - 1}} & B < 10 \\ (1 - 0.0858 e^{-0.0617(B-10)}) & B \geq 10 \end{cases}
$$

$$
\times \left(1 - \frac{\ln \frac{z_{\mathrm{o}}}{z_{\mathrm{os}}}}{\ln(0.35 \left(\frac{10\mathrm{cm}}{z_{\mathrm{os}}} \right)^{0.8})} \right)^{-1}
$$

$$
\times \sqrt{1 + 1.21 \max(0, \left(w - (0.0014 \phi_{\mathrm{clay}}^2 + 0.17 \phi_{\mathrm{clay}}) \right))^{0.68}}, \tag{A1}
$$

where

$D_{\mathrm{p}} = 60\ \mu m$ saltation particle diameter

ρ_{air} air density

$\rho_{\mathrm{p}} = 2.65\ \mathrm{g/cm^3}$ particle density

$B = \frac{u_{*t} D_{\mathrm{p}}}{v}$ friction Reynolds number,

     initially $B = 1331 (D_{\mathrm{p}}/\mathrm{cm})^{1.56} + 0.38$

$v = 0.157 \cdot 10^{-4}\ \mathrm{m^2/s}$ kinematic viscosity of air

$z_{\mathrm{o}} = 0.01\ \mathrm{cm}$ surface roughness length

$z_{\mathrm{os}} = 0.00333\ \mathrm{cm}$ local roughness length of the uncovered surface

w gravimetric soil moisture in %

ϕ_{clay} clay fraction in %

The last, soil moisture term in Eq. (A1) is omitted in the present study. If the surface friction velocity u_* exceeds the threshold

5   u_{*t}, the resulting emission flux is computed according to the equation

$$j_{\mathrm{emis}} = \frac{c \rho_{\mathrm{air}}}{g} (u_* + u_{*t})^2 (u_* - u_{*t})\ 10^{-4}\ a\ f_{\mathrm{landcover}}\ f_{\mathrm{veg}}, \tag{A2}$$

where

$c = 1$ empirical constant (in this study $c = 1.5$)

$g = 9.80665\ \mathrm{m/s^2}$ gravitational acceleration

u_* surface friction velocity

$f_{\mathrm{landcover}}$ barren land fraction

$f_{\mathrm{veg}} = 1 - \frac{\min(\mathrm{LAI}, 0.35)}{0.35}$ vegetation factor

a sandblasting efficiency

10   In the present study we multiply the right-hand side of Eq. (A2) with the topography factor $S_{\mathrm{topo}} = ((z_{\max} - z)/(z_{\max} - z_{\min}))^5$ defined in Eq. (3) and the corresponding normalisation factor $N = 5.3$. In addition, the surface friction velocity u_* is limited to a maximal valure of $0.4\ \mathrm{m/s}$, i.e., u_* in Eq. (A2) is replaced by $\min(u_*, 0.4\ \mathrm{m/s})$.

References

M. Abdelkader, S. Metzger, R. E. Mamouri, M. Astitha, L. Barrie, Z. Levin, and J. Lelieveld. Dust–air pollution dynamics over the eastern Mediterranean. *Atmospheric Chemistry and Physics*, 15(16):9173–9189, 2015. doi:10.5194/acp-15-9173-2015. URL http://www.atmos-chem-phys.net/15/9173/2015/.

5 M. Abdelkader, S. Metzger, B. Steil, K. Klingmüller, H. Tost, A. Pozzer, G. Stenchikov, L. Barrie, and J. Lelieveld. Chemical aging of atmospheric mineral dust during transatlantic transport. *Atmospheric Chemistry and Physics Discussions*, 2016:1–36, 2016. doi:10.5194/acp-2016-470. URL http://www.atmos-chem-phys-discuss.net/acp-2016-470/.

AERONET. http://aeronet.gsfc.nasa.gov. visited 31 Aug 2016.

Anatolii Anisimov, Weichun Tao, Georgiy Stenchikov, Stoitchko Kalenderski, P. Jish Prakash, Zong-Liang Yang, and Mingjie Shi. Quan-
10 tifying local-scale dust emission from the arabian red sea coastal plain. *Atmospheric Chemistry and Physics*, 17:993–1015, 1 2017. doi:10.5194/acp-17-993-2017.

M. Astitha, J. Lelieveld, M. Abdel Kader, A. Pozzer, and A. de Meij. Parameterization of dust emissions in the global atmospheric chemistry-climate model EMAC: impact of nudging and soil properties. *Atmospheric Chemistry and Physics*, 12(22):11057–11083, 2012. doi:10.5194/acp-12-11057-2012.

15 Yves Balkanski, Michael Schulz, Tanguy Claquin, Cyril Moulin, and Paul Ginoux. *Global Emissions of Mineral Aerosol: Formulation and Validation using Satellite Imagery*, pages 239–267. Springer Netherlands, Dordrecht, 2004. ISBN 978-1-4020-2167-1. doi:10.1007/978-1-4020-2167-1_6. URL http://dx.doi.org/10.1007/978-1-4020-2167-1_6.

Gordon B. Bonan, Samuel Levis, Laurent Kergoat, and Keith W. Oleson. Landscapes as patches of plant functional types: An integrating concept for climate and ecosystem models. *Global Biogeochemical Cycles*, 16(2):5–1–5–23, 2002. ISSN 1944-9224.
20 doi:10.1029/2000GB001360. URL http://dx.doi.org/10.1029/2000GB001360.

H. Brindley, S. Osipov, R. Bantges, A. Smirnov, J. Banks, R. Levy, P. Jish Prakash, and G. Stenchikov. An assessment of the quality of aerosol retrievals over the red sea and evaluation of the climatological cloud-free dust direct radiative effect in the region. *Journal of Geophysical Research: Atmospheres*, 120:10, 10 2015. doi:10.1002/2015JD023282.

C. Clerbaux, A. Boynard, L. Clarisse, M. George, J. Hadji-Lazaro, H. Herbin, D. Hurtmans, M. Pommier, A. Razavi, S. Turquety, C. Wespes,
25 and P.-F. Coheur. Monitoring of atmospheric composition using the thermal infrared IASI/MetOp sounder. *Atmospheric Chemistry and Physics*, 9(16):6041–6054, 2009. doi:10.5194/acp-9-6041-2009.

Guillaume A. d'Almeida. On the variability of desert aerosol radiative characteristics. *Journal of Geophysical Research*, 92(D3):3017, 1987. doi:10.1029/JD092iD03p03017.

Jeffrey J. Danielson and Dean B. Gesch. Global Multi-resolution Terrain Elevation Data 2010 (GMTED2010). *U.S. Geological Survey
30 Open-File Report*, (2011—1073), 2011. URL http://pubs.usgs.gov/of/2011/1073/pdf/of2011-1073.pdf.

Kremena Darmenova, Irina N. Sokolik, Yaping Shao, Beatrice Marticorena, and Gilles Bergametti. Development of a physically based dust emission module within the Weather Research and Forecasting (WRF) model: Assessment of dust emission parameterizations and input parameters for source regions in Central and East Asia. *Journal of Geophysical Research: Atmospheres*, 114:D14201, 2009. doi:10.1029/2008JD011236.

35 C. Fountoukis and A. Nenes. ISORROPIA II: a computationally efficient thermodynamic equilibrium model for K^+-Ca^{2+}-Mg^{2+}-NH_4^+-Na^+-SO_4^{2-}-NO_3^--Cl^--H_2O aerosols. *Atmospheric Chemistry and Physics*, 7(17):4639–4659, 2007. doi:10.5194/acp-7-4639-2007. URL http://www.atmos-chem-phys.net/7/4639/2007/.

D. Giannadaki, A. Pozzer, and J. Lelieveld. Modeled global effects of airborne desert dust on air quality and premature mortality. *Atmospheric Chemistry and Physics*, 14(2):957–968, 2014. doi:10.5194/acp-14-957-2014. URL http://www.atmos-chem-phys.net/14/957/2014/.

Paul Ginoux, Mian Chin, Ina Tegen, Joseph M. Prospero, Brent Holben, Oleg Dubovik, and Shian-Jiann Lin. Sources and distributions of dust aerosols simulated with the GOCART model. *Journal of Geophysical Research: Atmospheres*, 106(D17):20255–20273, 2001. doi:10.1029/2000JD000053.

G. Gläser, A. Kerkweg, and H. Wernli. The Mineral Dust Cycle in EMAC 2.40: sensitivity to the spectral resolution and the dust emission scheme. *Atmospheric Chemistry and Physics*, 12(3):1611–1627, 2012. doi:10.5194/acp-12-1611-2012. URL http://www.atmos-chem-phys.net/12/1611/2012/.

GMTED2010. https://lta.cr.usgs.gov/GMTED2010, 2010. visited 24 Aug 2016.

Fiona Hilton, Raymond Armante, Thomas August, Chris Barnet, Aurelie Bouchard, Claude Camy-Peyret, Virginie Capelle, Lieven Clarisse, Cathy Clerbaux, Pierre-Francois Coheur, Andrew Collard, Cyril Crevoisier, Gaelle Dufour, David Edwards, Francois Faijan, Nadia Four-rié, Antonia Gambacorta, Mitchell Goldberg, Vincent Guidard, Daniel Hurtmans, Samuel Illingworth, Nicole Jacquinet-Husson, Tobias Kerzenmacher, Dieter Klaes, Lydie Lavanant, Guido Masiello, Marco Matricardi, Anthony McNally, Stuart Newman, Edward Pavelin, Sebastien Payan, Eric Péquignot, Sophie Peyridieu, Thierry Phulpin, John Remedios, Peter Schlüssel, Carmine Serio, Larrabee Strow, Claudia Stubenrauch, Jonathan Taylor, David Tobin, Walter Wolf, and Daniel Zhou. Hyperspectral Earth Observation from IASI: Five Years of Accomplishments. *Bulletin of the American Meteorological Society*, 93:347–370, 2012. doi:10.1175/BAMS-D-11-00027.1.

B.N. Holben, T.F. Eck, I. Slutsker, D. Tanré, J.P. Buis, A. Setzer, E. Vermote, J.A. Reagan, Y.J. Kaufman, T. Nakajima, F. Lavenu, I. Jankowiak, and A. Smirnov. AERONET—A Federated Instrument Network and Data Archive for Aerosol Characterization. *Remote Sensing of Environment*, 66(1):1–16, 1998. doi:10.1016/S0034-4257(98)00031-5.

P. Hubanks, S. Platnick, M. King, and B. Ridgway. *MODIS Atmosphere L3 Gridded Product Algorithm Theoretical Basis Document (ATBD) & Users Guide*, 2015.

N. Huneeus, M. Schulz, Y. Balkanski, J. Griesfeller, J. Prospero, S. Kinne, S. Bauer, O. Boucher, M. Chin, F. Dentener, T. Diehl, R. Easter, D. Fillmore, S. Ghan, P. Ginoux, A. Grini, L. Horowitz, D. Koch, M. C. Krol, W. Landing, X. Liu, N. Mahowald, R. Miller, J.-J. Morcrette, G. Myhre, J. Penner, J. Perlwitz, P. Stier, T. Takemura, and C. S. Zender. Global dust model intercomparison in aerocom phase i. *Atmospheric Chemistry and Physics*, 11:7781–7816, 8 2011. doi:10.5194/acp-11-7781-2011.

IASI. http://www.esa-aerosol-cci.org/. visited 31 Aug 2016.

IPCC, editor. *Climate Change 2013 – The Physical Science Basis*. Cambridge University Press, 2014. ISBN 9781107415324. URL http://dx.doi.org/10.1017/CBO9781107415324. Cambridge Books Online.

P. Jöckel, R. Sander, A. Kerkweg, H. Tost, and J. Lelieveld. Technical Note: The Modular Earth Submodel System (MESSy) - a new approach towards Earth System Modeling. *Atmospheric Chemistry and Physics*, 5(2):433–444, 2005. doi:10.5194/acp-5-433-2005. URL http://www.atmos-chem-phys.net/5/433/2005/.

P. Jöckel, A. Kerkweg, A. Pozzer, R. Sander, H. Tost, H. Riede, A. Baumgaertner, S. Gromov, and B. Kern. Development cycle 2 of the Modular Earth Submodel System (MESSy2). *Geoscientific Model Development*, 3(2):717–752, 2010. doi:10.5194/gmd-3-717-2010. URL http://www.geosci-model-dev.net/3/717/2010/.

V. A. Karydis, A. P. Tsimpidi, A. Pozzer, M. Astitha, and J. Lelieveld. Effects of mineral dust on global atmospheric nitrate concentrations. *Atmospheric Chemistry and Physics*, 16:1491–1509, 2 2016. doi:10.5194/acp-16-1491-2016.

L. Kergoat, Moulin S., Cayrol P., and Dedieu G. Controlling vegetation growth models with satellite measurements. In Blasco F. and Weill A., editors, *Advances in environmental and ecological modelling*, pages 73–89. Elsevier Publishers, 1999.

K. Klingmüller, B. Steil, C. Brühl, H. Tost, and J. Lelieveld. Sensitivity of aerosol radiative effects to different mixing assumptions in the AEROPT 1.0 submodel of the EMAC atmospheric-chemistry–climate model. *Geoscientific Model Development*, 7(5):2503–2516, 2014. doi:10.5194/gmd-7-2503-2014.

K. Klingmüller, A. Pozzer, S. Metzger, G. L. Stenchikov, and J. Lelieveld. Aerosol optical depth trend over the Middle East. *Atmospheric Chemistry and Physics*, 16(8):5063–5073, 2016. doi:10.5194/acp-16-5063-2016. URL http://www.atmos-chem-phys.net/16/5063/2016/.

B. Laurent, B. Marticorena, G. Bergametti, J. F. Léon, and N. M. Mahowald. Modeling mineral dust emissions from the Sahara desert using new surface properties and soil database. *Journal of Geophysical Research: Atmospheres*, 113(D14):n/a–n/a, 2008. ISSN 2156-2202. doi:10.1029/2007JD009484. URL http://dx.doi.org/10.1029/2007JD009484. D14218.

B. Laurent, I. Tegen, B. Heinold, K. Schepanski, B. Weinzierl, and M. Esselborn. A model study of Saharan dust emissions and distributions during the SAMUM-1 campaign. *Journal of Geophysical Research: Atmospheres*, 115(D21):n/a–n/a, 2010. ISSN 2156-2202. doi:10.1029/2009JD012995. URL http://dx.doi.org/10.1029/2009JD012995. D21210.

R. C. Levy, S. Mattoo, L. A. Munchak, L. A. Remer, A. M. Sayer, F. Patadia, and N. C. Hsu. The collection 6 modis aerosol products over land and ocean. *Atmospheric Measurement Techniques*, 6(11):2989–3034, 2013. doi:10.5194/amt-6-2989-2013.

B. Marticorena and G. Bergametti. Modeling the atmospheric dust cycle: 1. Design of a soil-derived dust emission scheme. *Journal of Geophysical Research*, 100(D8):16415, 1995. doi:10.1029/95JD00690.

B. Marticorena, G. Bergametti, B. Aumont, Y. Callot, C. N'Doumé, and M. Legrand. Modeling the atmospheric dust cycle: 2. Simulation of Saharan dust sources. *Journal of Geophysical Research: Atmospheres*, 102(D4):4387–4404, 1997. ISSN 2156-2202. doi:10.1029/96JD02964. URL http://dx.doi.org/10.1029/96JD02964.

S. Metzger, N. Mihalopoulos, and J. Lelieveld. Importance of mineral cations and organics in gas-aerosol partitioning of reactive nitrogen compounds: case study based on MINOS results. *Atmospheric Chemistry and Physics*, 6(9):2549–2567, 1 2006. doi:10.5194/acp-6-2549-2006.

S. Metzger, B. Steil, M. Abdelkader, K. Klingmüller, L. Xu, J. E. Penner, C. Fountoukis, A. Nenes, and J. Lelieveld. Aerosol water parameterisation: a single parameter framework. *Atmospheric Chemistry and Physics*, 16(11):7213–7237, 2016. doi:10.5194/acp-16-7213-2016. URL http://www.atmos-chem-phys.net/16/7213/2016/.

MODIS MCD12C1. ftp://ladsweb.nascom.nasa.gov/allData/51/MCD12C1/. visited 9 Jun 2016.

MODIS MOD08 M3. ftp://ladsweb.nascom.nasa.gov/allData/6/MOD08_M3/. visited 24 May 2017.

Natural Earth. http://www.naturalearthdata.com, 2016. visited 16 Nov 2016.

J. Olson. World Ecosystems (WE1.4): Digital raster data on a 10 minute geographic 1080 x 2160 grid. In *Global Ecosystems Database, version 1.0, Disc A*. NOAA National Geophysical Data Center, Boulder, Colorado, 1992.

C. Pérez, S. Nickovic, J. M. Baldasano, M. Sicard, F. Rocadenbosch, and V. E. Cachorro. A long Saharan dust event over the western Mediterranean: Lidar, Sun photometer observations, and regional dust modeling. *Journal of Geophysical Research: Atmospheres*, 111 (D15):n/a–n/a, 2006. ISSN 2156-2202. doi:10.1029/2005JD006579. URL http://dx.doi.org/10.1029/2005JD006579. D15214.

Thomas Popp, Gerrit de Leeuw, Christine Bingen, Christoph Brühl, Virginie Capelle, Alain Chedin, Lieven Clarisse, Oleg Dubovik, Roy Grainger, Jan Griesfeller, Andreas Heckel, Stefan Kinne, Lars Klüser, Miriam Kosmale, Pekka Kolmonen, Luca Lelli, Pavel Litvinov, Linlu Mei, Peter North, Simon Pinnock, Adam Povey, Charles Robert, Michael Schulz, Larisa Sogacheva, Kerstin Stebel, Deborah Stein Zweers, Gareth Thomas, Lieuwe Tilstra, Sophie Vandenbussche, Pepijn Veefkind, Marco Vountas, and Yong Xue. Development, Production and Evaluation of Aerosol Climate Data Records from European Satellite Observations (Aerosol_cci). *Remote Sensing*, 8: 421–, 2016. doi:10.3390/rs8050421.

K. J. Pringle, H. Tost, S. Message, B. Steil, D. Giannadaki, A. Nenes, C. Fountoukis, P. Stier, E. Vignati, and J. Lelieveld. Description and evaluation of GMXe: a new aerosol submodel for global simulations (v1). *Geoscientific Model Development*, 3:391, 9 2010a. doi:10.5194/gmd-3-391-2010.

K. J. Pringle, H. Tost, S. Metzger, B. Steil, D. Giannadaki, A. Nenes, C. Fountoukis, P. Stier, E. Vignati, and J. Lelieveld. Corrigendum to "description and evaluation of GMXe: a new aerosol submodel for global simulations (v1)" published in geosci. model dev., 3, 391-412, 2010. *Geoscientific Model Development*, 3:413, 9 2010b. doi:10.5194/gmd-3-413-2010.

A. M. Sayer, L. A. Munchak, N. C. Hsu, R. C. Levy, C. Bettenhausen, and M.-J. Jeong. Modis collection 6 aerosol products: Comparison between aqua's e-deep blue, dark target, and "merged" data sets, and usage recommendations. *Journal of Geophysical Research: Atmospheres*, 119(24):13,965–13,989, 2014. doi:10.1002/2014JD022453.

R.J. Scholes and E. Brown de Colstoun. ISLSCP II Global Gridded Soil Characteristics. In Forrest G. Hall, G. Collatz, B. Meeson, S. Los, E. Brown de Colstoun, and D. Landis, editors, *ISLSCP Initiative II Collection*. ORNL Distributed Active Archive Center, 2011. doi:10.3334/ORNLDAAC/1004. URL http://dx.doi.org/10.3334/ORNLDAAC/1004.

Wei Shangguan, Yongjiu Dai, Qingyun Duan, Baoyuan Liu, and Hua Yuan. A global soil data set for earth system modeling. *Journal of Advances in Modeling Earth Systems*, 6(1):249–263, 2014. ISSN 1942-2466. doi:10.1002/2013MS000293. URL http://dx.doi.org/10.1002/2013MS000293.

Mingjie Shi, Zong-Liang Yang, Georgiy L. Stenchikov, Sagar P. Parajuli, Weichun Tao, and Stoitchko Kalenderski. Quantifying the impacts of landscape heterogeneity and model resolution on dust emissions in the arabian peninsula. *Environmental Modelling & Software*, 78:106–119, 1 2016. doi:10.1016/j.envsoft.2015.12.021.

S. Solomos, A. Ansmann, R.-E. Mamouri, I. Binietoglou, P. Patlakas, E. Marinou, and V. Amiridis. Remote sensing and modeling analysis of the extreme dust storm hitting Middle East and Eastern Mediterranean in September 2015. *Atmospheric Chemistry and Physics Discussions*, 2016:1–31, 2016. doi:10.5194/acp-2016-1006. URL http://www.atmos-chem-phys-discuss.net/acp-2016-1006/.

C. Spyrou, C. Mitsakou, G. Kallos, P. Louka, and G. Vlastou. An improved limited area model for describing the dust cycle in the atmosphere. *Journal of Geophysical Research: Atmospheres*, 115(D17):n/a–n/a, 2010. ISSN 2156-2202. doi:10.1029/2009JD013682. URL http://dx.doi.org/10.1029/2009JD013682. D17211.

D. Tanre, J.-F. Geleyn, and J. M. Slingo. First results of the introduction of an advanced aerosol-radiation interaction in the ECMWF low resolution global model. In H.E. Gerber and A. Deepak, editors, *Aerosols and their climatic effects*, pages 133–177. A. Deepak Pub., 1984. ISBN 9780937194065.

Karl E. Taylor. Summarizing multiple aspects of model performance in a single diagram. *Journal of Geophysical Research: Atmospheres*, 106(D7):7183–7192, 2001. doi:10.1029/2000JD900719.

Ina Tegen. Impact of vegetation and preferential source areas on global dust aerosol: Results from a model study. *Journal of Geophysical Research*, 107(D21):4576, 2002. doi:10.1029/2001JD000963.

B. R. White. Soil transport by winds on Mars. *Journal of Geophysical Research*, 84:4643–4651, 1979. doi:10.1029/JB084iB09p04643.

Hua Yuan, Yongjiu Dai, Zhiqiang Xiao, Duoying Ji, and Wei Shangguan. Reprocessing the MODIS Leaf Area Index products for land surface and climate modelling. *Remote Sensing of Environment*, 115(5):1171 – 1187, 2011. ISSN 0034-4257. doi:http://dx.doi.org/10.1016/j.rse.2011.01.001. URL http://www.sciencedirect.com/science/article/pii/S0034425711000149.

Charles S. Zender, Huisheng Bian, and David Newman. Mineral Dust Entrainment and Deposition (DEAD) model: Description and 1990s dust climatology. *Journal of Geophysical Research: Atmospheres*, 108(D14):n/a–n/a, 2003. ISSN 2156-2202. doi:10.1029/2002JD002775. URL http://dx.doi.org/10.1029/2002JD002775. 4416.
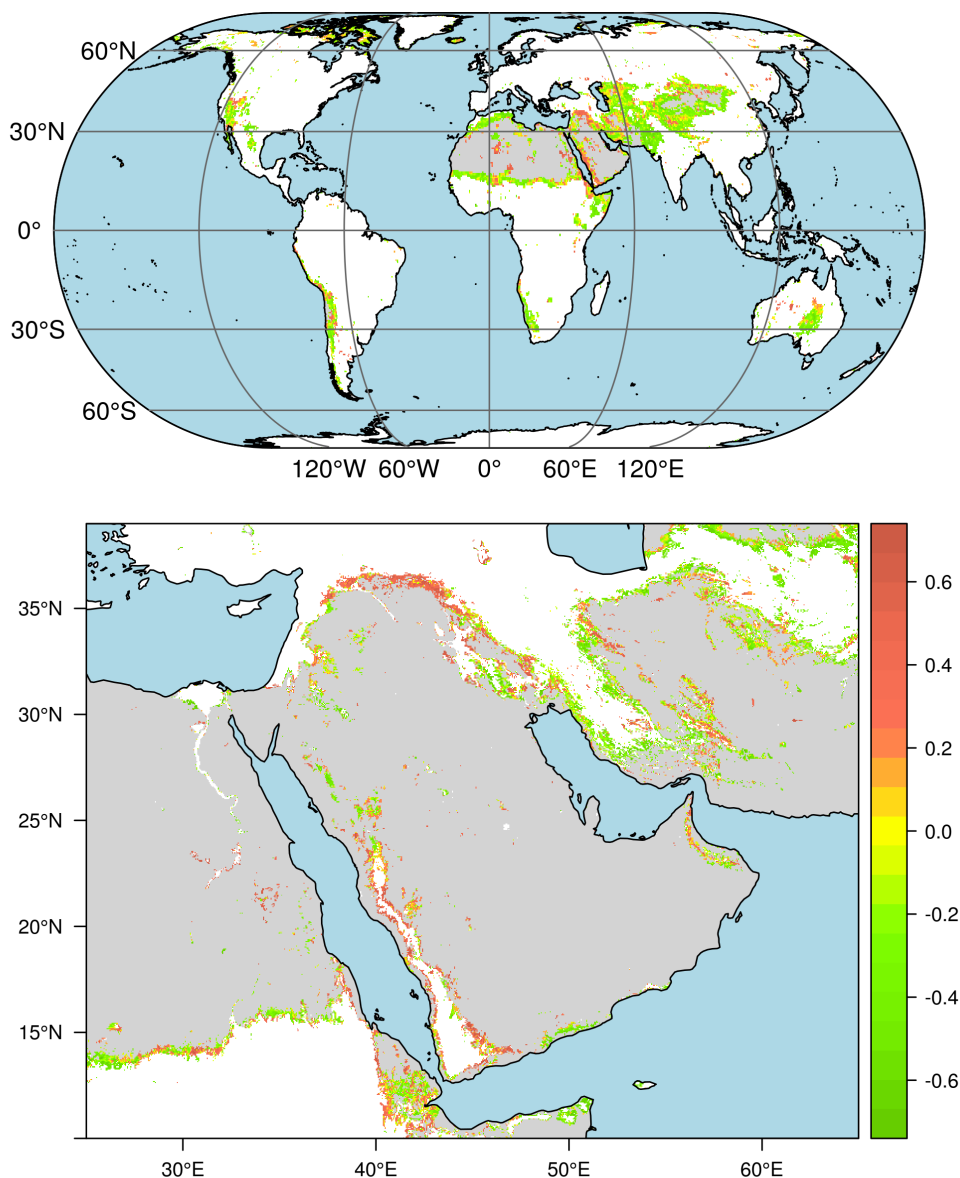
Figure 1. Trend of the dust emission mask based on the MODIS MCD12C1 landcover product during the period 2001 to 2012. Regions with changing surface properties are coloured according to the Kendall rank correlation coefficient τ of time and mask value, depicting expansion of source regions (i.e., positive correlation coefficients) in red, and contraction in green. Regions where the land cover remained unchanged are grey (source regions) or white (non-source regions). For better readability, in the global plot (top) the values have been averaged over 10 by 10 pixels ignoring constant pixels. The magnified plot of the Middle East (bottom) shows the original $0.05°$ pixels.
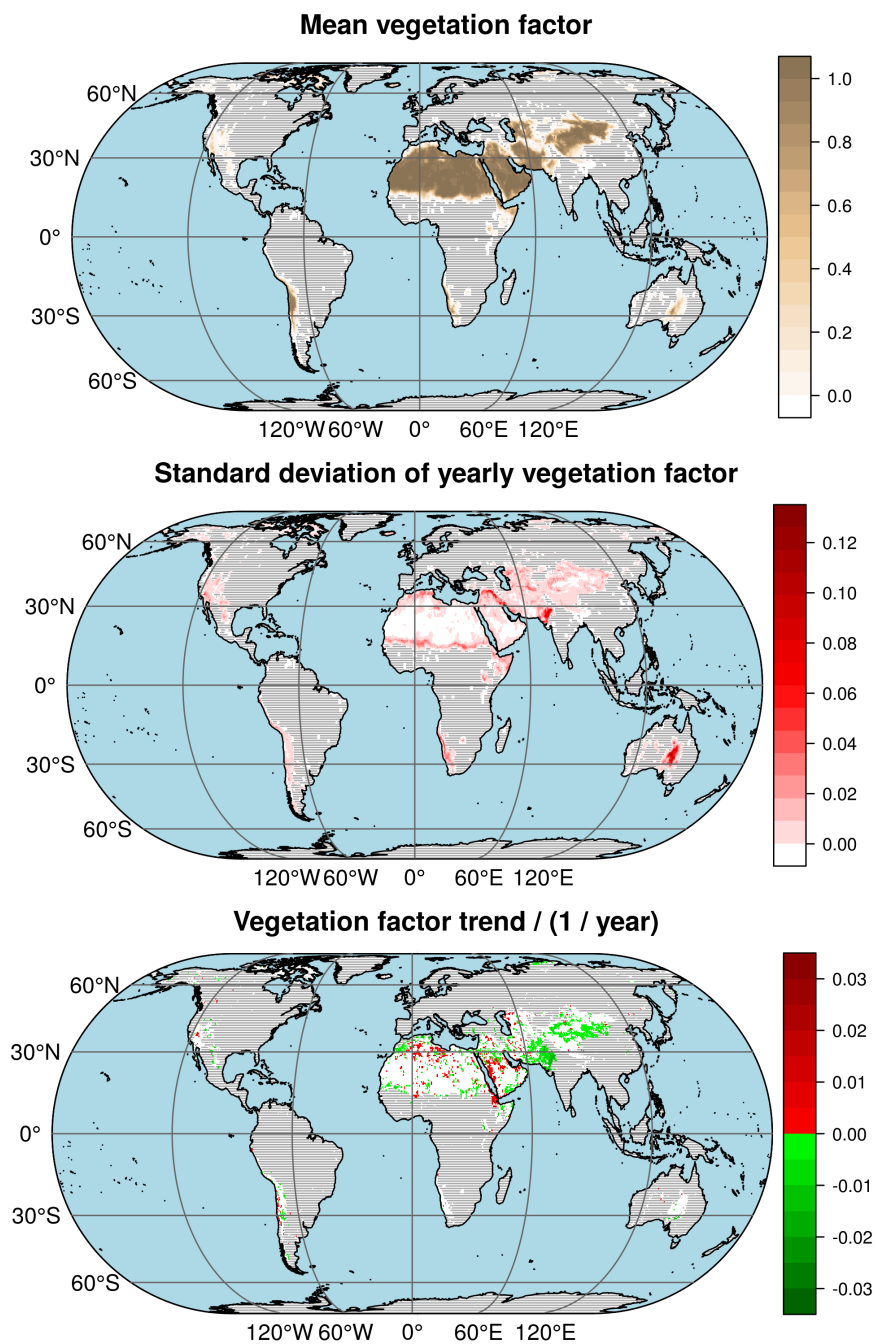
Figure 2. Vegetation factor based on leaf area index data from Yuan et al. (2011) averaged over the period 2000 to 2015 (top), the standard deviation of the annual mean values (center) and the trend of the annual mean values (bottom). Regions where the landcover mask precludes emissions throughout the period of available landcover data (2001 to 2012) are hatched.
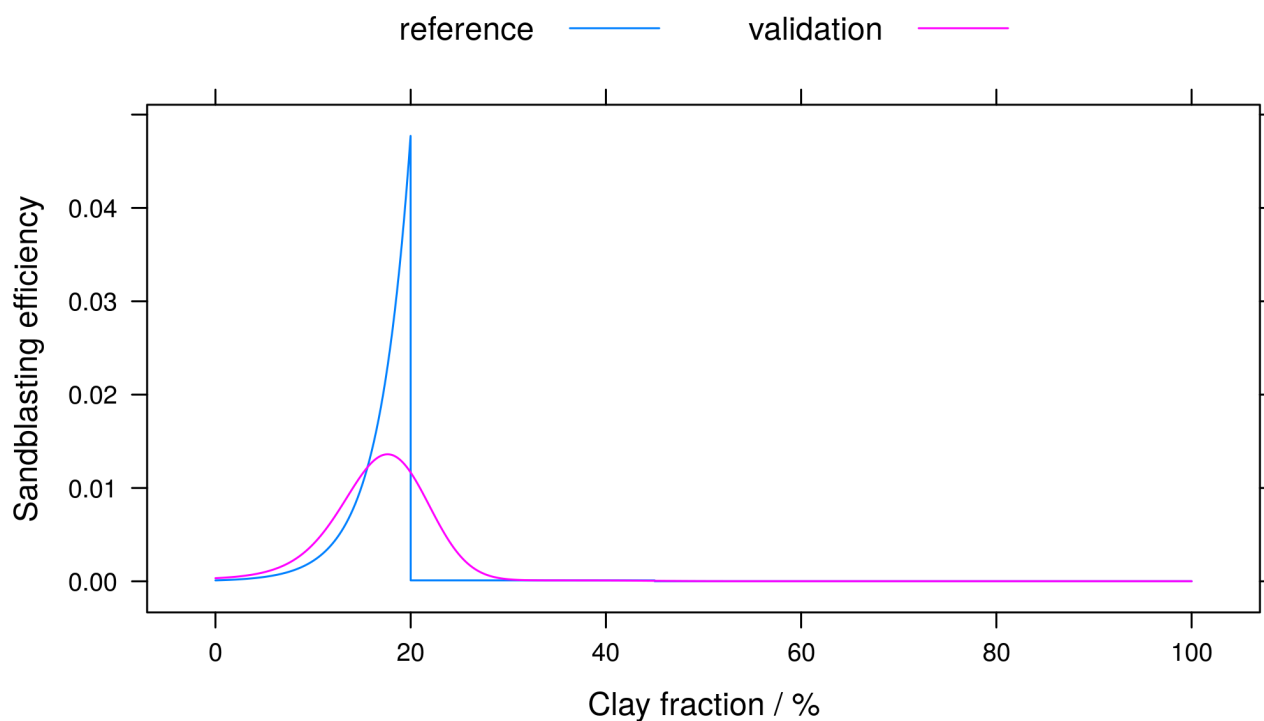
Figure 3. The sandblasting efficiency as function of the clay fraction used by Astitha et al. (2012), before ("reference") and after ("valida-tion") applying a Gaussian filter with an interquartile range of 5 %.
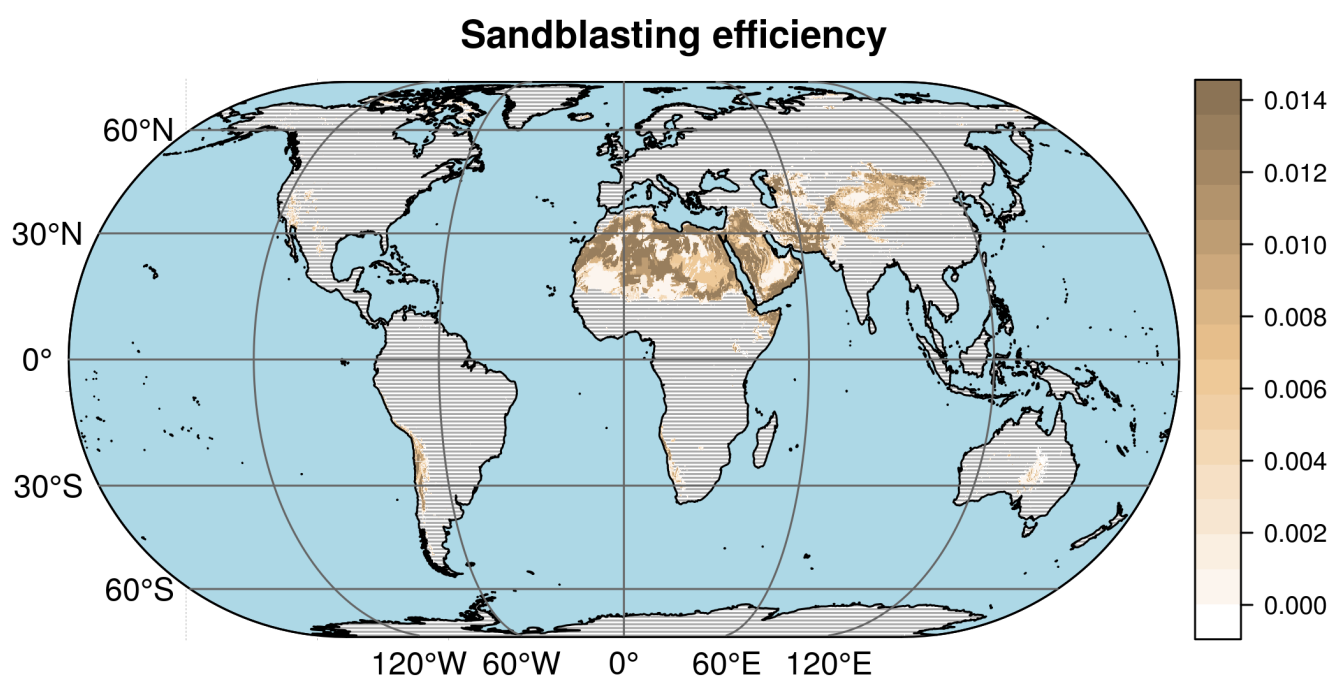
Figure 4. Global map of the sandblasting efficiency obtained by applying the filtered efficiency function shown in Fig. 3 to the GSDE clay fraction data. Regions where the landcover mask precludes emissions throughout the period of available landcover data (2001 to 2012) are hatched.
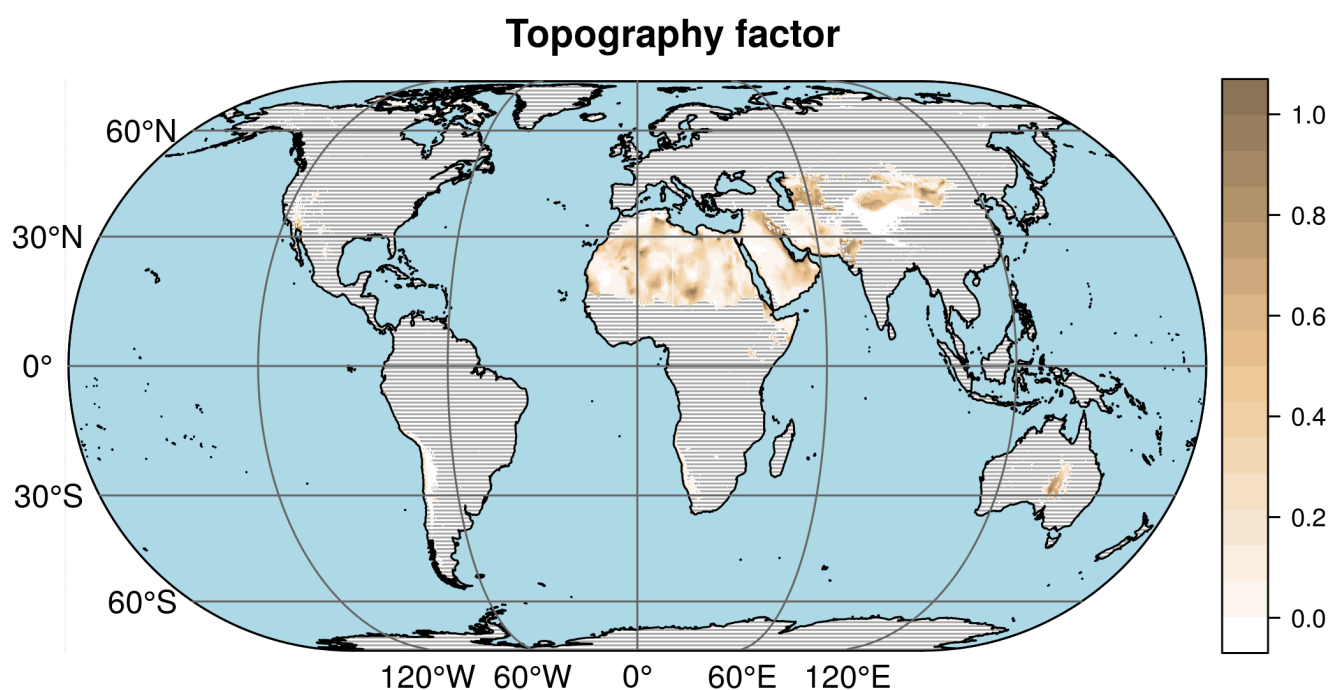
Figure 5. The topography factor defined by Eq. 3, calculated using the GMTED2010 elevation data. Regions where the landcover mask precludes emissions throughout the period of available landcover data (2001 to 2012) are hatched.
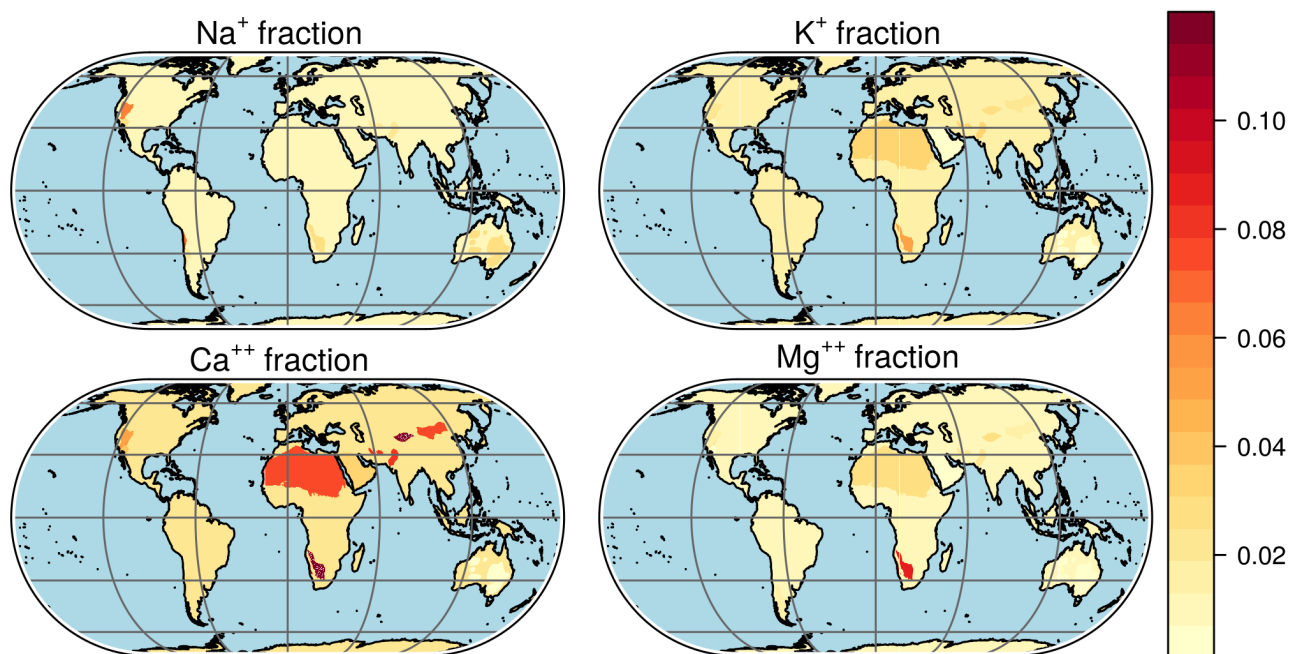
Figure 6. Maps of the Na$^+$, K$^+$, Ca^{++} and Mg^{++} fractions of the soil of different desert regions, used to calculate the chemical composition of the emitted dust particles.
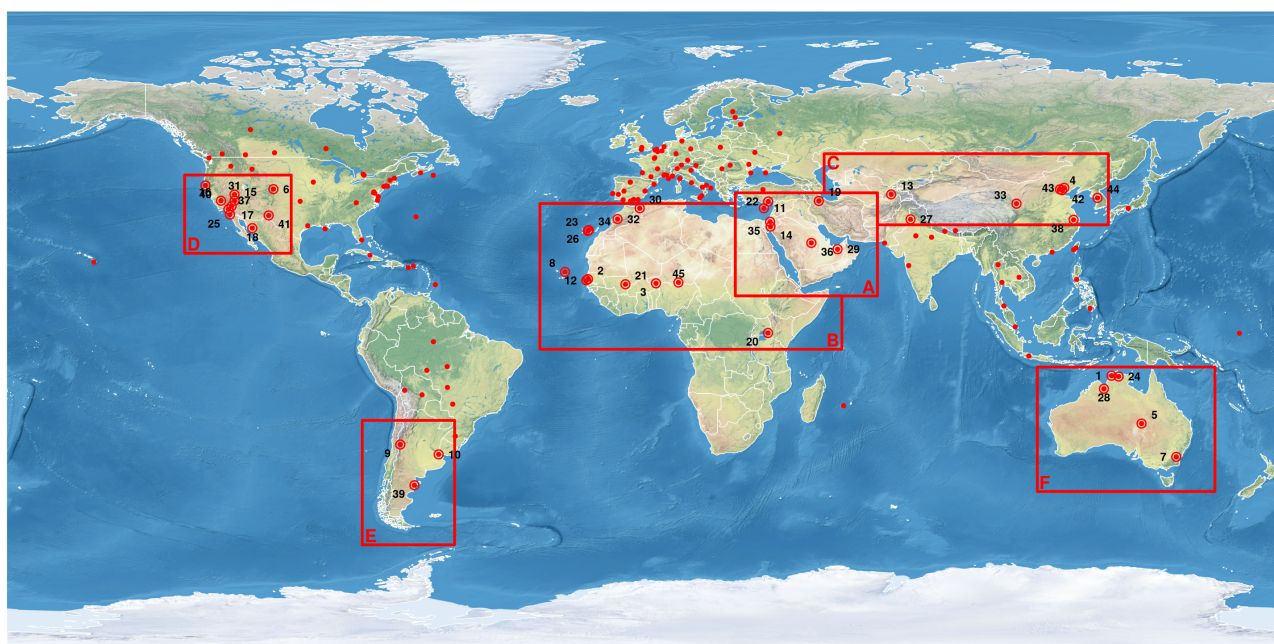
1 ARM_Darwin	10 CEILAP-BA	19 IASBS	28 Lake_Argyle	37 TABLE_MOUNTAIN_CA
2 Bambey-ISRA	11 CUT-TEPAK	20 ICIPE-Mbita	29 Mezaira	38 Taihu
3 Banizoumbou	12 Dakar	21 IER_Cinzana	30 Oujda	39 Trelew
4 Beijing	13 Dushanbe	22 IMS-METU-ERDEMLI	31 Railroad_Valley	40 Trinidad_Head
5 Birdsville	14 Eilat	23 Izana	32 Saada	41 White_Sands_HELSTF
6 BSRN_BAO_Boulder	15 Frenchman_Flat	24 Jabiru	33 SACOL	42 XiangHe
7 Canberra	16 Fresno	25 La_Jolla	34 Santa_Cruz_Tenerife	43 Xinglong
8 Capo_Verde	17 Goldstone	26 La_Laguna	35 SEDE_BOKER	44 Yonsei_University
9 CASLEO	18 Hermosillo	27 Lahore	36 Solar_Village	45 Zinder_Airport

Figure 7. AERONET stations and regions of interest (A to F) used for the evaluation. Stations with data for 120 or more days distributed over at least 9 months of 2011 (red dots) are considered, yielding 45 stations within the regions of interest (labelled).
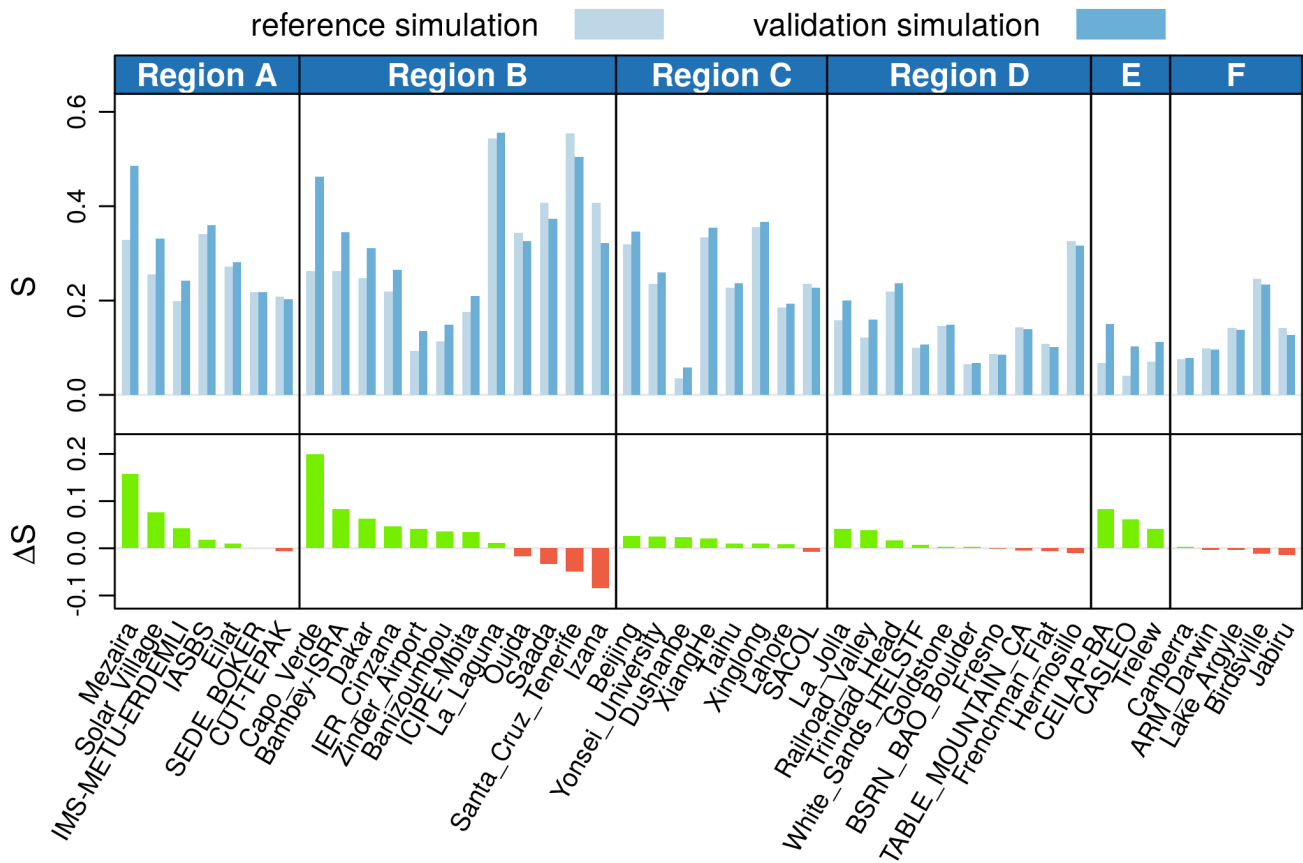
Figure 8. Skill score S of the daily mean 550 nm AOD from reference and validation simulations using AERONET observations as benchmark. The red and green bars depict the differences between reference and validation values, with green bars indicating that the validation results agree more closely with the measurements. Generally, the validation simulation performs better than the reference simulation; regarding the decreased skill scores in north-west Africa, please refer to the discussion in the main text.
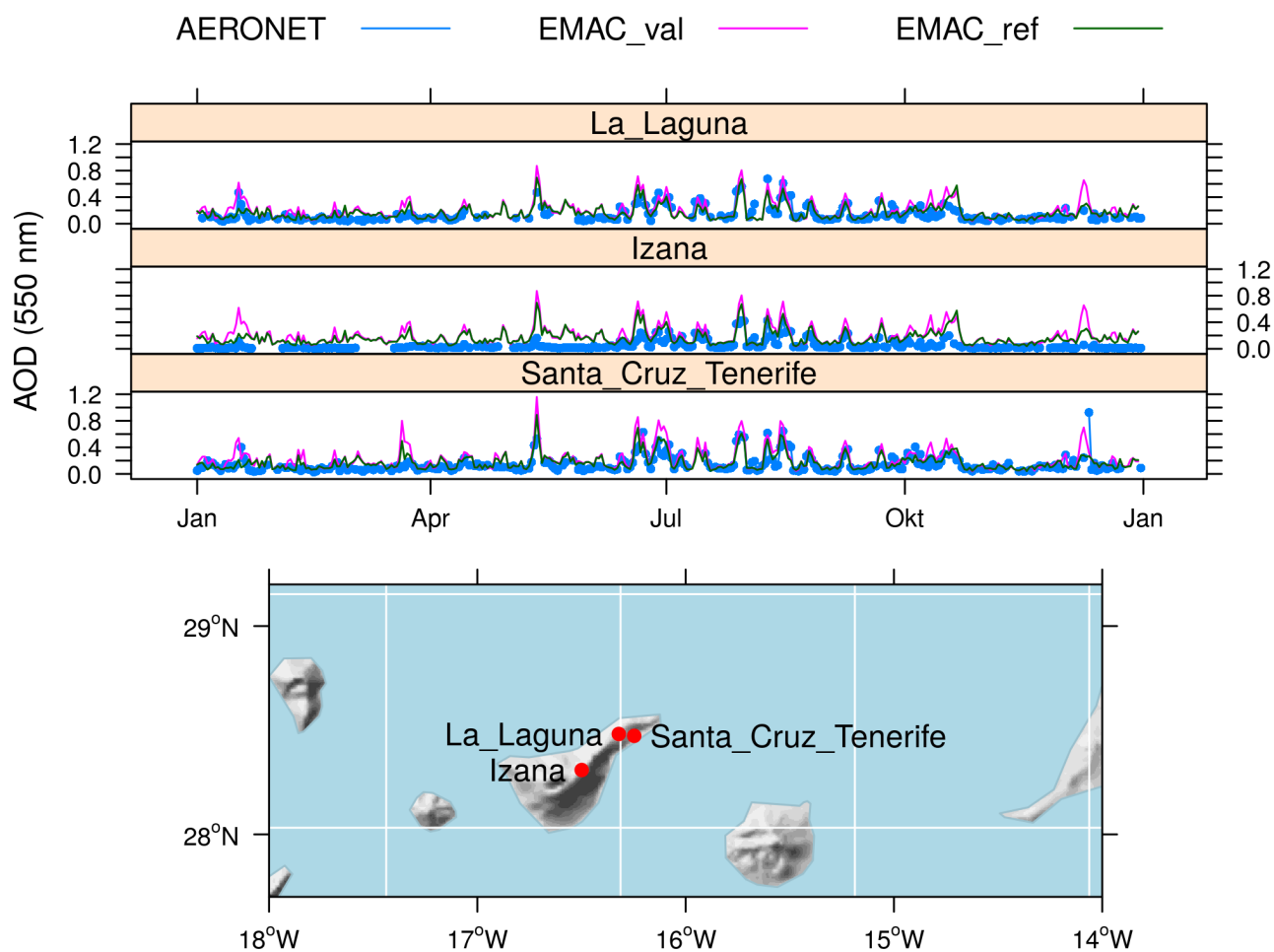
Figure 9. Time series of the daily mean AOD at the Canarian AERONET stations (top) and a map showing the location of the stations (bottom). The white grid depicts the T106 model grid.
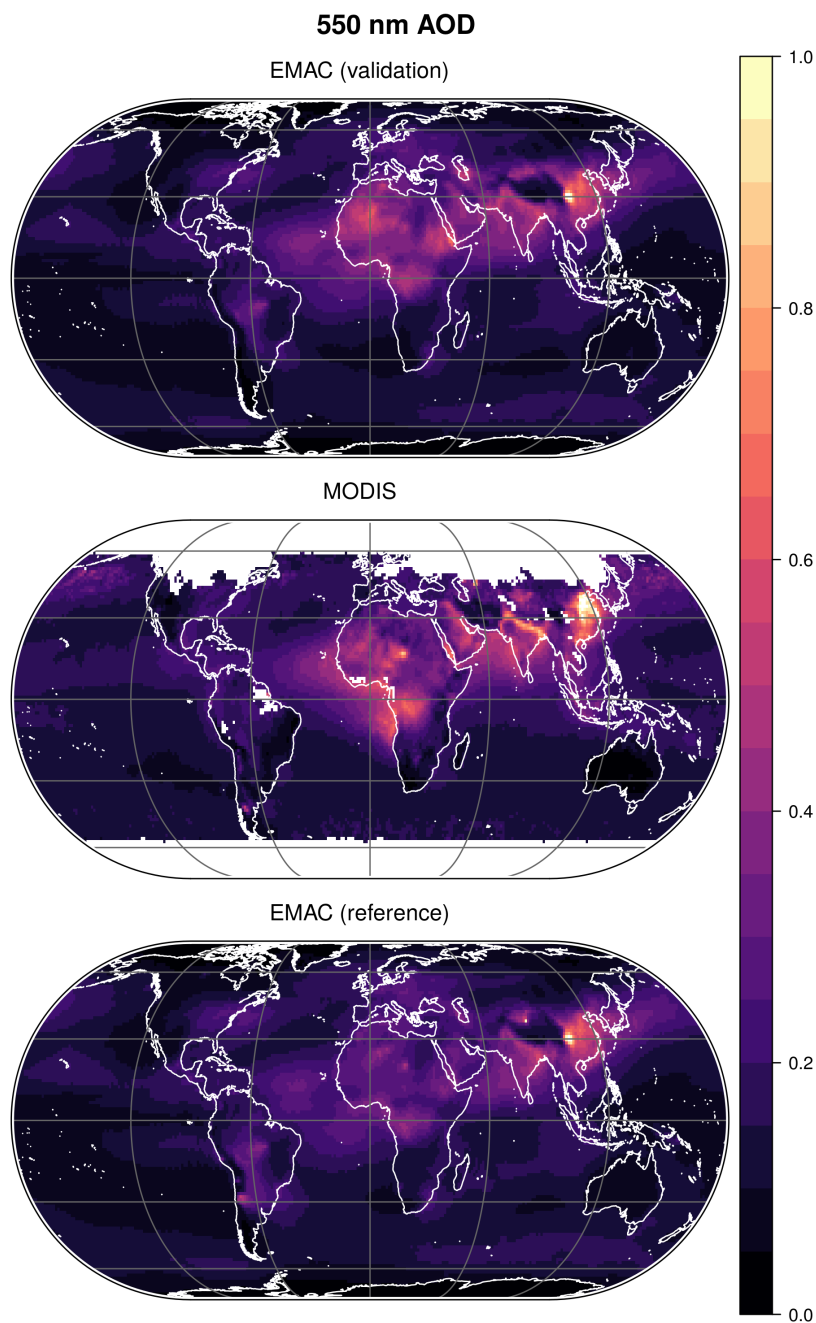
Figure 10. Annual mean for 2011 of the AOD at 550 nm wavelength observed by MODIS (centre) and simulated by EMAC with ("valida-tion", top) and without ("reference", bottom) revision of the dust emission scheme. The revised dust emissions enhance the correlation of the AOD pattern from 0.79 to 0.81, the skill score from 0.58 to 0.67.
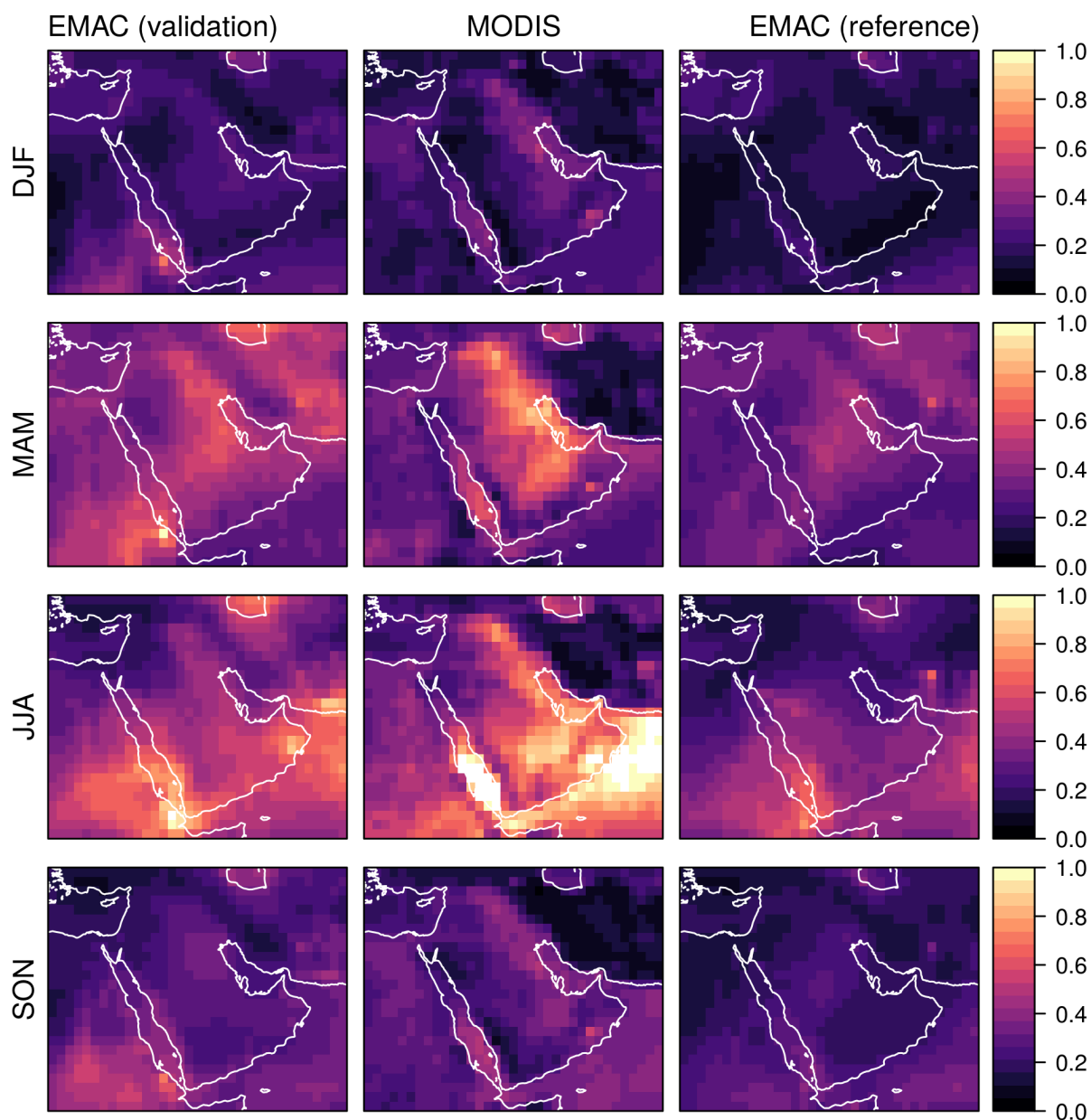
Figure 11. Seasonal 550 nm AOD over the Middle East (region of interest A) in 2011 observed by MODIS (centre column) and simulated by EMAC with ("validation", left) and without ("reference", right) revision of the dust emission scheme. Each row shows the three-month averages over the periods (from top to bottom) DJF (December, January, February), MAM (March, April, May), JJA (June, July, August) and SON (September, October, November).
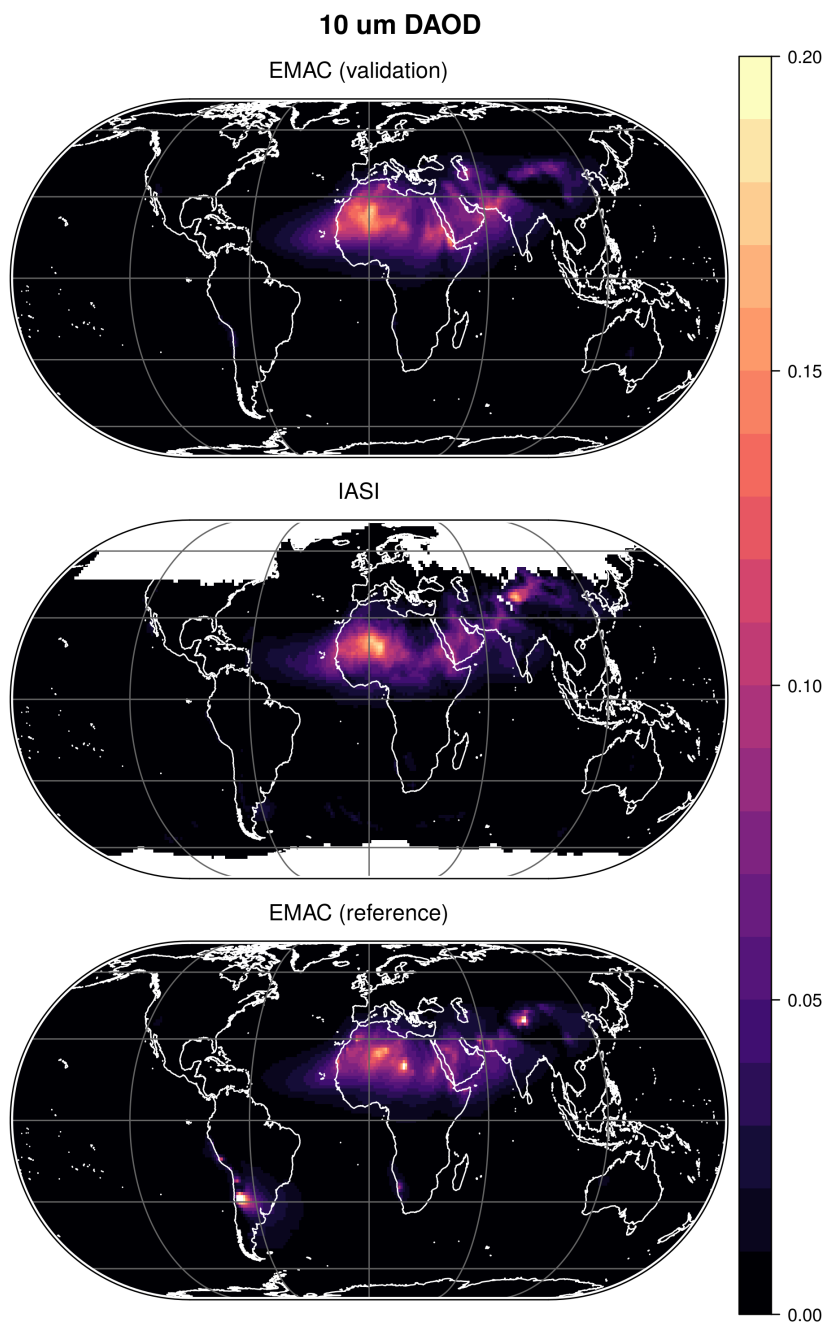
Figure 12. Annual mean for 2011 of the DAOD at 10 μm wavelength observed by IASI (centre) and simulated by EMAC with ("validation", top) and without ("reference", bottom) revision of the dust emission scheme. The revised dust emissions enhance the correlation of the AOD pattern from 0.79 to 0.89, the skill score from 0.64 to 0.78.

10000 nm DAOD
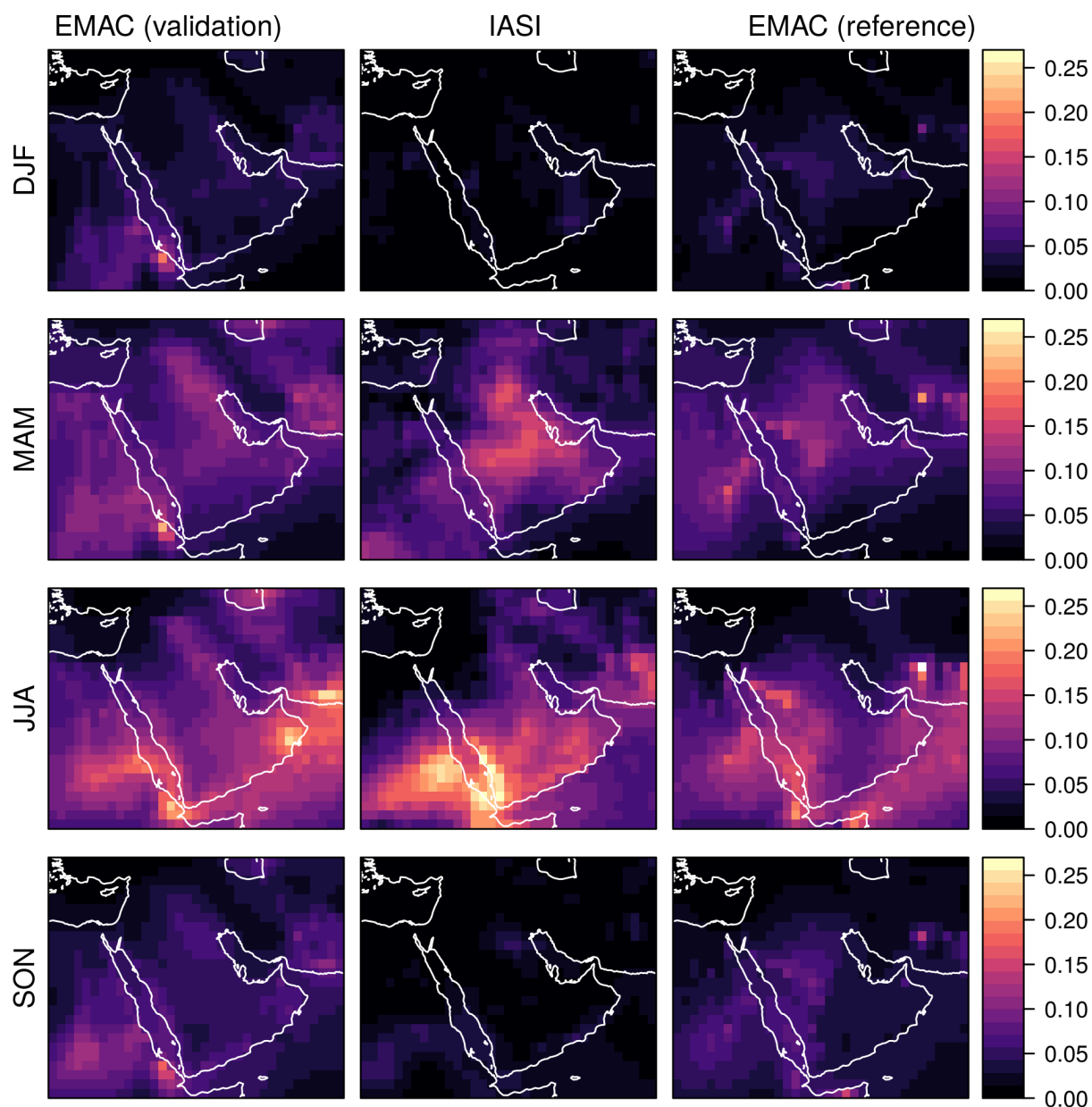
Figure 13. Seasonal 10 μm DAOD over the Middle East (region of interest A) in 2011 observed by IASI (centre column) and simulated by EMAC with ("validation", left) and without ("reference", right) revision of the dust emission scheme. Each row shows the three-month averages over the periods (from top to bottom) DJF (December, January, February), MAM (March, April, May), JJA (June, July, August) and SON (September, October, November).

Table 1. Summary of updated and added input data

		Reference input data	Updated/new input data
Land cover	Source	Olson (1992)	MODIS MCD12C1
	Spatial resolution	1°(aggregated from 10')	0.05°
	Temporal resolution	static	yearly data (since 2001)
Clay fraction	Source	Scholes and Brown de Colstoun (2011)	GSDE (Shangguan et al., 2014)
	Spatial resolution	1°	0.1°(aggregated from 30")
	Temporal resolution	static	static
	Notes	clay fraction in top 30 cm soil layer	clay fraction in top 4.5 cm soil layer
Vegetation	Source	Kergoat et al. (1999); Bonan et al. (2002)	Yuan et al. (2011)
	Spatial resolution	1°(aggregated from 0.5°)	0.1°(aggregated from 30")
	Temporal resolution	monthly values (Apr 1992 to Mar 1993)	monthly values (since 2000, aggregated from 8 day values)
	Notes		MODIS based
Topography	Source	-	Danielson and Gesch (2011); GMTED2010 (2010)
	Spatial resolution	-	0.1°(aggregated from 30")
	Temporal resolution	-	static
Chemical composition	Source	-	Karydis et al. (2016); Natural Earth (2016)
	Spatial resolution	-	0.1°
	Temporal resolution	-	static

Table 2. Parameters of emission and GMXE dust modes. The GMXE parameter values shown have been used for reference and validation simulation.

	σ_g	$\tilde{d}/\mu\mathrm{m}$	$d_{\min}/\mu\mathrm{m}$
Emission modes	2.1	0.83	
	1.9	4.82	
	1.6	19.4	
GMXE dust modes	1.59		0.12
	2		2

Table 3. Global mineral dust emissions in 2011 obtained by EMAC.

	Validation simulation	Reference simulation
Accumulation mode	0.148 Gt / year	0.0517 Gt / year
Coarse mode	1.16 Gt / year	1.28 Gt / year
Total	1.31 Gt / year	1.33 Gt / year